Journal of Quantitative Spectroscopy & Radiative Transfer 203 (2017) 565–571

Contents lists available at ScienceDirect

Journal of Quantitative Spectroscopy & Radiative Transfer

journal homepage: www.elsevier.com/locate/jqsrt

O_2 nightglow snapshots of the 1.27 μm emission at low latitudes on Mars with a static field-widened Michelson interferometer

Zhang Rui[a,b,*], William E. Ward [b], Zhang Chunmin[a]

[a] Institute of Space Optics, School of Science, Xi'an Jiaotong University, 28 Xianning West Road, 710049, Xi'an, Shaanxi, China
[b] Department of Physics, University of New Brunswick, 8 Bailey Drive, NB, E3B 5A3, Fredericton, Canada

ARTICLE INFO

Article history:
Received 16 January 2017
Received in revised form
10 August 2017
Accepted 10 August 2017
Available online 12 August 2017

Keywords:
Interferometry
Dynamics observation
Martian atmosphere
Nightglow
Remote sensing

ABSTRACT

A static field-widened Michelson interferometer is designed to observe the atmospheric dynamics at low latitudes of Mars, targeting the 1.27 μm $O_2(a^1\Delta_g)$ nightglow, which has not yet been accurately detected due to its low intensity. To the best of our knowledge, this design is the first demonstration of implementing divided-mirror technique by refringent materials in a field-widened Michelson interferometer. Different optical path difference (OPD) in each quadrant is generated by four highly reflective pyramid-shaped prisms made of different refringent materials attached to each solid arm of Michelson interferometer. In this way four samples of interferogram are obtained simultaneously, from which the airglow volume emission rate, as well as the line-of-sight velocity and temperature of the air parcel where the emission forms can be derived in a single integration time. To achieve the best field-widening, compactness and thermal compensation, all possible combination of ten pieces of glasses were searched within the Sumita glass catalogue using a computer program and some interesting results are listed. The OPD used in this calculation concerns rays in the plane perpendicular to the sides of the prism only, other cases need further examination. This instrument's performance in measuring atmospheric dynamics is analysed, using the wind velocity uncertainty as primary criterion. Calculations show that it can measure the wind with an accuracy better than 2 m/s if the band volume emission rate of O_2 nightglow is greater than 5 kph cm^{-3} s^{-1}.

1. Introduction

The field-widened Michelson interferometer stems from the Michelson interferometer but is used in a very different way: measuring the Doppler shift of a single spectral line as well as its linewidth. It works in the optical path difference (OPD) space rather than spectral space and is designed specifically for weak airglow emissions, therefore its application often goes into atmospheric dynamics observations, measuring wind, temperature, constituent variation etc. Some successful designs and implementations of such instrument includes the Wind Imaging Interferometer (WINDII) on board NASA's Upper Atmosphere Research Satellite (UARS) measuring winds in the range of 80–300 km altitude [1–3]; the E-region wind interferometer (ERWIN) measuring upper atmospheric winds at three altitudes near the mesopause using airglow emissions O(^{1}S), OH, and O_2 [4–5]; The Stratospheric Wind Interferometer For Transport Studies (SWIFT) for global stratospheric dynamics and the transport of ozone [6]; Michelson Interferometer for Airglow Dynamics Imaging (MIADI) for buoyancy wave observations in airglow in the mesopause region of the terrestrial atmosphere [7].

Such field-widened Michelson interferometers usually have compensating glasses in each arm to achieve the field-widening, achromatic and thermal compensation conditions and a scanning mirror to sequentially sample the interferogram, from which the wind, temperature and constituent information can be derived. One of the problems that arise in the detection of very small phase shifts by the sequential sampling of the interferogram is the possibility of intensity variations of the source during the course of a measurement [8]. Hence in the 1990's the divided-mirror technique was explored at York University. Field-widened Michelson interferometers incorporating this technique usually have one mirror divided into four quadrants each coated by a reflective thin film multilayers [9] to generate optical path difference (usually 1/4 wavelength between quadrants). In this way four images are taken simultaneously, reducing the effect of any emission variations on the calculated phase. The measurement will also be insensitive to any thermal drift within the instrument as long as the duration of each wind determination is more rapid than any temporal variation of the thermal background [10]. Field-widened Michelson interferometers using this divided-mirror technique include the Mesospheric Imaging Michelson interferometer measuring the

* Corresponding author.
E-mail address: ruizhangphysics@outlook.com (R. Zhang).

http://dx.doi.org/10.1016/j.jqsrt.2017.08.009
0022-4073/

Mesospheric wind from the ground [11] and the Waves Michelson Interferometer (WaMI) and provide simultaneous measurements of dynamical and constituent signatures in the upper stratosphere, mesosphere and lower thermosphere [10].

In this paper, an alternative way to implement divided-mirror technique in a field-widened Michelson interferometer is presented. Refringent materials such as glass are used to create optical path difference in each quadrant replacing the thin film multilayers used in earlier designs [9–11]. This gains us an additional degree of freedom in field-widening and thermally compensating the Michelson while maintaining the advantage that the instrument has no moving parts. The constraint in the divided-mirror technique that the optical path difference between quadrants should be 1/4 wavelength (90° phase difference) is released in our design. We show that wind phase can still be derived when phase difference between samples are slightly off 90° This instrument is intended to measure the volume emission rate of atomic oxygen, wind, and temperature at low and middle latitude of Mars by observing the $O_2(a^1\Delta_g)$ nightglow. The following section selects target lines for measurement, the next one describes the design concept and optical layout of the instrument. This is followed by the calculation of optical path difference (OPD) and glass selection process and discussions. The instrument behaviours are then examined for the current design by estimating wind measurement uncertainty. The paper closes with a summary of the potential of this instrument and what remains for future research.

2. Line selection

The 1.27μm emission of O_2 airglow in the upper atmosphere of Mars is produced by photo-dissociation of ozone on the day side, and recombination of atomic oxygen on the night side [12]. The dayglow was first detected by Noxon in the 1970s from ground-based observation [13] and then confirmed by Krasnopolsky and others. Its spatial and seasonal variations through entire Martian year were monitored from the orbit, using SPICAM and OMEGA spectrometers on Mars Express and CRISM on Mars Reconnaissance Orbiter, as a sensitive tracer for high-altitude ozone abundance [14–15]. The nightglow, however, was detected quite recently and only in the subpolar regions where the emission is bright and the conditions are extreme. The first direct observation is provided by OMEGA/Mars Express observing at the limb close to southern and northern Poles at polar night in 2010 [16], and later confirmed by the CRISM experiment on Mars Reconnaissance Orbiter [17]. An attempt to measure the 1.27μm O_2 nightglow at low and middle altitudes on Mars was made by Krasnopolsky in 2013 using the ground-based NASA infrared Telescope Facility (IRTF) yielding 10 ± 32kR [12]. Muñoz's model [18] shows that the O_2 nightglow is distributed from 40 km to 80 km altitude, with a peak at 62 km. The peak Band Volume Emission Rate (BVER) is estimated to be around 20 kph cm^{-3} s^{-1}. BVER above and below 40 km at selected times is shown in Fig. 1.

Calculation shows that the radiative lifetime for O_2 $(a^1\Delta_g)$ is about 4470 s [17]. Its long lifetime ensures that the oxygen atoms are in thermal equilibrium with the surrounding atmosphere. After thousands of collisions with the surrounding atmospheric molecules, the natural width of the line is small and could be safely neglected, so the observed shape arises solely from the Doppler shifts associated with the Maxwellian velocity distribution and can be represented by a Gaussian.

The structure of the O_2 $(a^1\Delta_g)$ band and the three lines chosen for observation are shown in Fig. 2 [19]. These three lines were chosen because they are relatively well separated from the neighboring lines and have distinct temperature sensitivities. However, it can be seen in Fig. 2 that between these three lines the spectral intervals are still small, their wavelengths differing by only a few angstroms. To optically isolate them before sending them into the Michelson, a filter combination is needed. The combination contains a broadband interference filter and a Fabry-Perot etalon. The input light will first transmit the broadband interference filter, whose width is usually set at 20Å, and then the

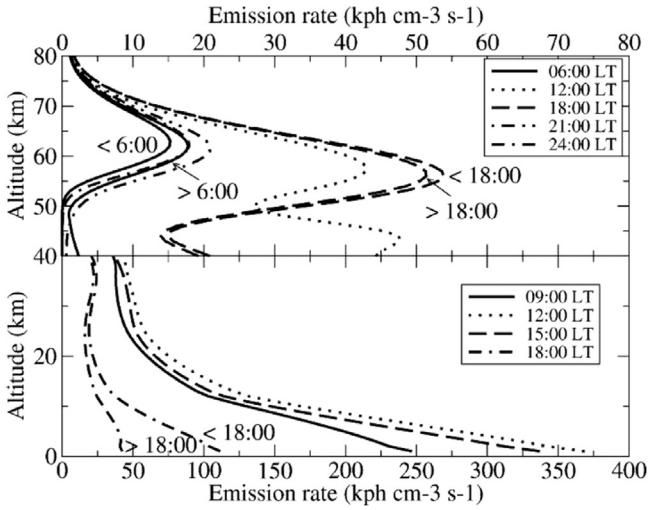

Fig. 1. Modeled BVER of the $O_2(a^1\Delta_g)$ 1.27 μm airglow at selected times. After Muñoz et al. [2005].

Fabry-Perot interferometer, which is to spatially separate the three lines in the angular field. The interferogram received at the detector has different rings corresponding to different lines formed onto different portions of the detector (charge-coupled device or CCD). This complicates the analysis but each ring (line) gives an independent value of wind velocity, so that is a benefit [20]. A similar filters combination was employed by WINDII for observing line $^PP(7)$ and $^PQ(7)$ in $O_2(b^1\sum)$ band, where the manufacturer provided a single cavity filter, creating an effective combined etalon/filter of 0.09 nm half-width [1]. For O_2 $(a^1\Delta_g)$ band, the details of filter design can be found in Babcock's thesis [11].

The emission lines parameters are summarized in Table 1 [19]. The three lines have similar relative intensity but their temperature sensitivities differ by more than an order of magnitude, thus satisfying our measurement requirements.

3. Mars imaging Michelson interferometer

The Mars Imaging Michelson Interferometer (MIMI) consists of an aperture stop, a filter, front and back telescopes with field stop placed inside, a solid-arm Michelson Interferometer (MI), a concave pyramid-shaped prisms, a camera lens, and a detector (Fig. 3).

The incoming light collected at the aperture stop is first sent into a filter combination to have the three selected lines isolated and then collimated by the front collecting telescope (Telescope 1). A field stop is placed in the telescope which defines the field of view (FOV). Telescope 1 focuses an image of the entrance aperture onto the end of each MI arm. At the end of each solid arm of the MI, four highly reflective pyramid-shaped prisms are attached (Fig. 3A) and divide the reflection surface into four sections. These eight prisms have highly reflective coatings on their sides and are made of glasses with different refractive indexes. Sorting the corresponding two in the same optical path into a pair, there are four pairs of prisms. By assigning a different refractive index difference to each pair, they will introduce four different OPDs to the instrument. The apex angle of the reflective prisms is set to 90° for the purpose that the collimated beams generated by the telescopes corresponding to the same point in the FOV will maintain collimated after being reflected by the prism and will be focused at the same point on the detector. This ensures that information from different points of the image do not interfere. The aperture imaging ensures that the light entering each of the four prisms is completely scrambled with respect to the FOV. This means that light from any part of the FOV contributes equally to each prism and therefore can be safely divided into four parts with no information lost or mistaken.

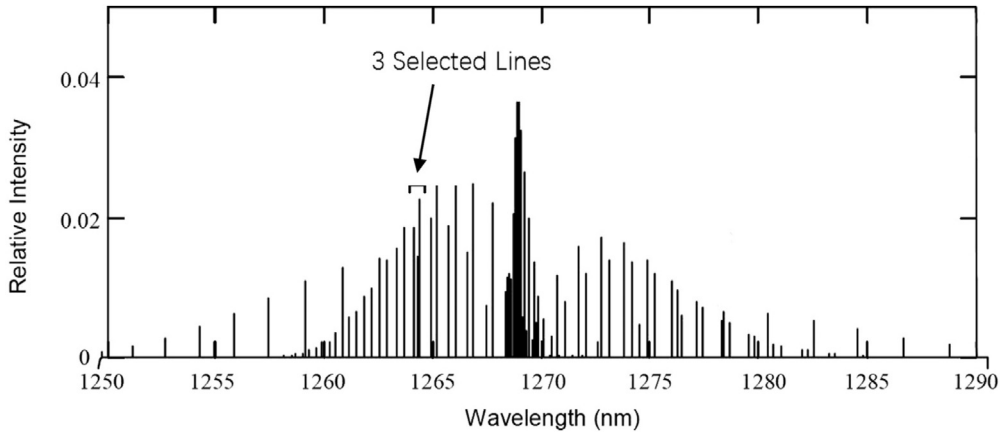

Fig. 2. O_2 ($a^1\Delta_g$) band for a temperature of 275 K. The selected lines are marked. The sum of relative intensities for the whole band is 1.00 [10].

Table 1
Selected lines for the $O_2(a^1\Delta_g)$ observations [19].

Emission	Line	Wavelength nm (air)	Relative Intensity (225 K)	dI/dT (225 K) %/K
O_2 ($a^1\Delta_g$)	$^RQ(9)$	1264.060	0.019	−0.016
	$^SR(3)$	1264.277	0.017	−0.34
	$^RR(9)$	1264.386	0.023	−0.016

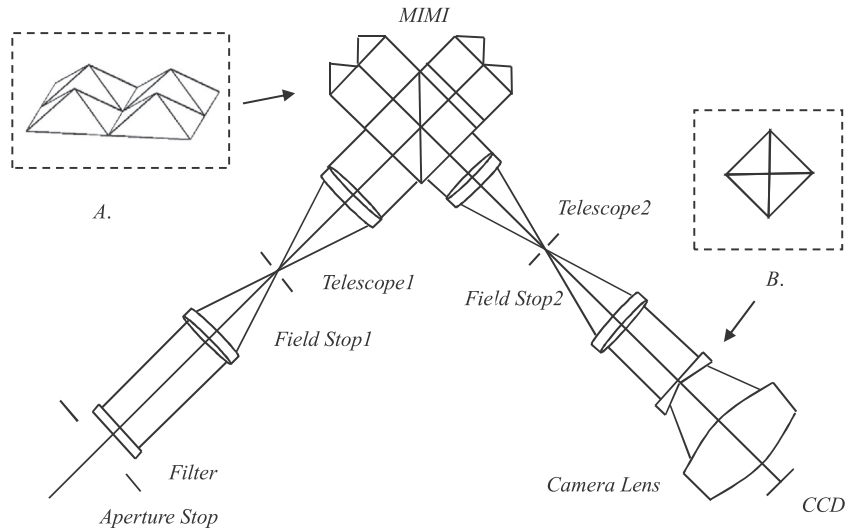

Fig. 3. Side view of MIMI. Input light passes through MIMI and forms four images on the CCD. By telescope 1 and 2, the aperture stop is imaged at the end of each arm and again at the flat face of pyramid prism. The field of view is imaged at the field stop 1, again at field stop 2, and a third time at the detector. (A) four reflective pyramid prisms, (B) Concave pyramid prism.

The reflected light will then be sent into telescope 2. The field stop in this back telescope is to help prevent stray light, including possible multiple reflections between the optics, from entering the detector. Telescope 2 will form image of aperture stop at the flat face of a concave, small base angle, right apex angle, pyramid-shaped prism (Fig. 3B), where the beam will be spatially separated into four. To focus these four beams onto corresponding sections of the detector, (each quadrant is imaged independently so the detector is also divided into four), the two opposite faces of the prism need to refract the incoming beams in different directions so one outgoing beam rotates clockwise from the initial orientation while the other rotates anticlockwise in the plane where the rays lie. This sets a constraint on the incident angle (i) so that it must be less than $n\theta$, where n is the refraction index of the prism and θ is its basic angle. We normally prefer θ to be small to reduce reflection and absorption loss while i to be large for better imaging and higher signal to noise ratio (SNR). The collecting lens before the CCD will then focus four replicated images of FOV onto different parts of the detector array. The lens is shown schematically in Fig. 3 as a simple lens, but for practical imaging, good quality lenses with the lowest possible aberrations and distortion are needed. A baffle in front of the entrance aperture is also necessary to prevent extraneous light scattering from optical surfaces, which may cause an unwanted background signal [21].

As can be seen from the design above, MIMI is stable and of low power consumption as it utilizes glass only. It is also monolithic and has no moving part, which reduces the risk of mechanical problems. These factors appropriately meet the requirement for spacecraft or satellite observations. Compensation is necessary for a field-widened Michelson interferometer to make successful measurement. This includes field-widening, achromatic and thermal compensation conditions and is usually achieved by selecting compensating glasses [22–23]. The next section will discuss the compensation process, using indices of refraction taken from the

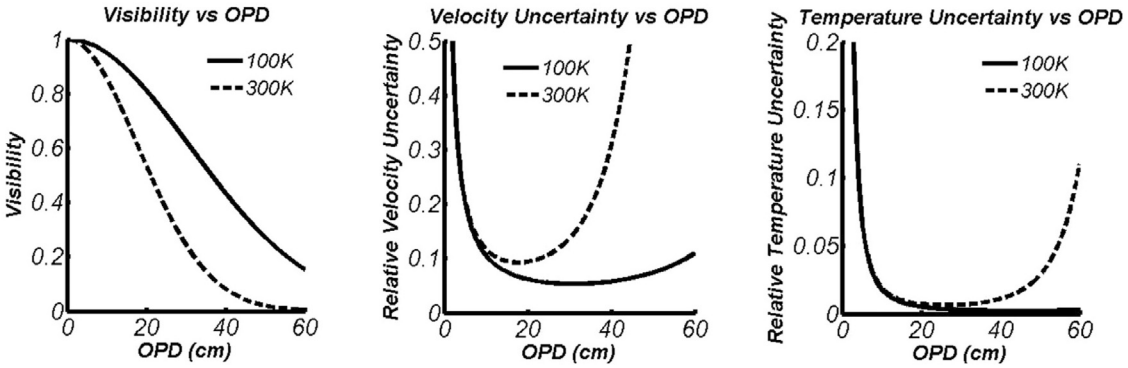

Fig. 4. Visibility, wind velocity uncertainty and temperature uncertainty variations with OPD.

Sumita glass catalogue. It should be noted that the actual implementation will depend on the measured index of refraction of the particular melt of the company, whose value can vary and might not exactly correspond to the calculated result.

4. Glass selection

10 pieces of glass in total need to be selected, including two pieces for Michelson arms and eight pieces for prisms attached to the arms. The beam splitter doesn't introduce OPD so we will not include discussion of its glass type for the moment. As Fig. 3 shows, the Michelson arms consist of two pieces of glass and an air gap with the glasses optically contacted. The first and principal task is to find the OPD of each section. For simplicity, we consider only the incoming rays that lie in the plane perpendicular to the side of the prism and calculate the OPDs between parallel rays in the four sections based on the geometry of the interferometer (Eq. 1), where Δ_k (k = A, B, C, D) denoting the OPD in four sections, n_1, n_2 the refractive index of the arm, n_{3k}, n_{4k} (k = A, B, C, D) the refraction index of the prisms, l the radius of the aperture and also the bottom length of the prism, d_1, d_2 the length of the arms, d_5 the length of the air gap, i_j (j = 1, 2, 3, 4, 5) the refraction angles in different media satisfying sin $i = n_1 sini_1 = n_2 sini_2 = n_3 sini_3 = n_4 sini_4 = n_5 sini_5$.

$$\begin{aligned}
\Delta_A &= (n_{4A}\cos i_{4A} - n_{3A}\cos i_{3A})l + 2n_2d_2\cos i_2 - 2n_1d_1\cos i_1 + 2d_5\cos i_5\\
\Delta_B &= (n_{4B}\cos i_{4B} - n_{3B}\cos i_{3B})l + 2n_2d_2\cos i_2 - 2n_1d_1\cos i_1 + 2d_5\cos i_5\\
\Delta_C &= (n_{4C}\cos i_{4C} - n_{3C}\cos i_{3C})l + 2n_2d_2\cos i_2 - 2n_1d_1\cos i_1 + 2d_5\cos i_5\\
\Delta_D &= (n_{4D}\cos i_{4D} - n_{3D}\cos i_{3D})l + 2n_2d_2\cos i_2 - 2n_1d_1\cos i_1 + 2d_5\cos i_5
\end{aligned} \quad (1)$$

Noticing that these equations contain a common term $2n_2d_2\cos i_2 - 2n_1d_1\cos i_1 + 2d_5\cos i_5$ and a variable term $(n_{4k}\cos i_{4k} - n_{3k}\cos i_{3k})l$ (k = A, B, C, D), the OPDs are set to vary around a definite value with the variations controlled within one or two fringes. To find a proper value for the common term of OPD, the variations of fringe visibility (Eq. (2)), wind uncertainty and temperature uncertainty with OPD are plotted (Fig. 4) using the approximated wind and temperature random error standard deviation [24] (Eqs. (3)–(4)). One could infer that the larger the OPD, the smaller the measurement uncertainty (to some extent) but against this is decreasing visibility. Our final choice is to set the OPD in the range of 10–15 cm.

$$V = exp\left(-2\pi^2 kT\Delta^2/\lambda^2 c^2 m\right) \quad (2)$$

$$\sigma(v) = c\lambda/\left(\sqrt{2nn_a\tau_f R_l \delta t I_0}\,\pi UV\Delta_\lambda\right) \quad (3)$$

$$\sigma(T) = \sqrt{2 + U^2V^2}/\left(\sqrt{nn_a\tau_f R_l \delta t I_0}\,Q_\lambda UV\Delta_\lambda^2\right) \quad (4)$$

The conditions that need to be met in the glass selection process are summarized below, including field-widening conditions, which requires that the angular dependence of OPD will only involve i^6 and higher terms (Eq. (5)); thermal compensation conditions, which requires the derivative of OPD with respect to temperature is zero, in which α denotes the thermal expansion coefficient (Eq. (6)); and compactness conditions, requiring that the arm lengths of MI should not exceed 15 cm. The achromatic condition is not necessary for this instrument as the three lines it measures are within a very small spectral range. Comparing Eqs. (1), (5) and (6) to the traditional compensation conditions for field-widened Michelson interferometer [20], one can find that the aperture diameter serves as an additional degree of freedom in determining OPD in our design. The field-widening and thermal compensation conditions therefore have this additional degree of freedom too as they depend on OPD. This adds flexibility in glass selection process as we have one more parameter to adjust when trying to meet all conditions simultaneously.

$$\begin{aligned}
&(1/n_{3k} - 1/n_{4k})l/2 - d_2/n_2 - d_5 + d_1/n_1 = 0\\
&(k = A,\ B, C, D)\ r\\
&\left(1/n_{3k}^3 - 1/n_{4k}^3\right)l/8 - d_2/4n_2^3 - d_5/4 + d_1/4n_1^3 = 0
\end{aligned} \quad (5)$$

$$\begin{aligned}
&\left(\frac{\partial n_{4k}}{\partial T} + \alpha_{4k}n_{4k} - \frac{\partial n_{3k}}{\partial T} - \alpha_{3k}n_{3k}\right)l\\
&\quad + 2d_2\left(\frac{\partial n_2}{\partial T} + \alpha_2 n_2\right)\\
&\quad -2d_1\left(\frac{\partial n_1}{\partial T} + \alpha_1 n_1\right) = 0\ (k = A, B, C, D)
\end{aligned} \quad (6)$$

Computer programs were used to put together all possible pairs of glasses in the Sumita Optical Glass Incorporation catalogue [25] which contains 116 different kinds of glasses. The program follows two steps. The first is to find four pairs of glass for the prisms whose refractive index's reciprocal difference, the cube of that, and thermal derivative difference give similar values (Table 2). The difference of the refractive index's reciprocal is made a priority in the search since it has the greatest influence in the field widening condition. The second step is to find the other two pieces of glass for the two arms (Table 3). The minimum acceptable refractive index difference in this case is set to be 0.3 to limit the arm lengths in the required range. An air gap is introduced to balance the deviation caused by the reflective prisms in the field-widening and thermal compensation conditions. The bottom length l of reflective prisms is specified to lie in the range of 2–4 cm for compactness as well as to keep the OPD at normal incidence close to the integral multiple of wavelength around 1.27μm. One interesting combination of ten pieces of glasses that meets all conditions to a good degree is shown in Table 4.

From Table 4 one can see that MIMI is compact as both arms are shorter than 13 cm and the area of the aperture is 18 cm^2. It is also insensitive to thermal drift as the derivative of OPD with respect to temperature is only 1.06e-5 cm K^{-1} or 0.08 of a wavelength K^{-1}. The

Table 2
Selected glass combination for eight prisms.

Number	Glass Pair	D(n)	D(1/n)	D(1/n^3)	D(∂n/∂T+αn)
1	K-LaSFn9/K-LaSFn10	0.001649	−0.00051	−0.00048	2.17E-07
	K-LaSKn1/K-VC82	0.001536	−0.00051	−0.00051	−2.88E-06
	K-LaFn2/K-LaFK55	0.001429	−0.00051	−0.00054	No data
	K-GIR79/K-VC99	0.001661	−0.00050	−0.00045	4.19E-06
2	K-LaKn2/K-SK18	0.002167	−0.00082	−0.00094	−1.68E-06
	K-BaF8/K-SSK9	0.002113	−0.00082	−0.00096	−2.92E-07
	K-PSKn2/K-SSK4	0.002053	−0.00080	−0.00093	−4.09E-06
	K-SK16/K-SSK9	0.002051	−0.00080	−0.00093	No data
3	K-BaF9/K-SK18RH	0.002539	−0.00096	−0.0011	−8.98E-07
	K-VC79/K-SK7	0.002433	–0.00096	–0.00113	3.26E-07
	K-PSKn2/K-SSK1	0.002451	–0.00095	–0.00112	−3.83E-06
	K-SK5/K-CSK120	0.002363	−0.00095	−0.00116	−2.36E-06
4	K-SSK1/K-SSK3	0.002898	−0.00113	−0.00133	−1.35E-06
	K-SK4/K-VC79	0.002885	−0.00113	−0.00133	−1.80E-06
	K-SK5/K-SKLD120	0.002802	−0.00113	−0.00137	−2.56E-06
	K-LaFn3/K-LaFn2	0.003179	−0.00113	−0.0012	No data

D(*) means difference between two items

Table 3
Selected glass combination for two arms.

Number	Glass Pair	D(n)	d_1(cm)	d_2(cm)
1	K-PG395/K-BOC20	0.327	14.04	14.248
2	K-PSK200/K-BOC20	0.36424	13.075	13.196
3	K-PSK100/K-BOC20	0.38495	12.658	12.723

field-widening condition is also well met. The calculated OPD variation with respect to incident angle relative to the OPD at normal incidence in four quadrants are plotted (Fig. 5), where the variation is calculated as a fraction of a wavelength (1.27 μm). The OPDs stay unchanged basically in all four quadrants when FOV is less than 8°, and change by less than 0.2 wavelengths when the FOV is extended to 15°. The OPD at normal incidence in each section is about 13.084 cm, staying within the range we set (10–15 cm).

5. Estimate of wind uncertainty

The primary factor in characterizing a field-widened Michelson Interferometer is the wind speed uncertainty [26]. The Michelson parameters described in the previous section must ensure the wind speed can be measured with an accuracy that will result in useful science even when observing a weak signal. In the case of MIMI, the wind velocity can be determined from the four samples of the interferogram over one integration time. The intensities received at the CCD corresponding to the same point in FOV that are duplicated in four images are calculated (Eq. (8)) assuming the differential emission function B(σ) of O_2 nightglow to be a Gaussian (Eq. (7)). Symbols used in these equations include σ, wavenumber, σ_0, central wavenumber, v, velocity along line of sight, c, speed of light, w, full width at half maximum (FWHM), Δ_k (k = A, B, C, D), OPD in each quadrant, V, emission line visibility due to the finite width of the observed emission line, which varies slightly in four sections, and U, instrumental visibility due to imperfections in the interferometer (which can be measured using a very narrow emission line as source, it is also different in four sections since light goes through different paths). The wind velocity v can then be derived using any three of the equations in Eq. (8), the result given here (Eq. (9)) used I_A, I_B and I_C.

$$B(\sigma) = B_0 \exp\left(-4ln2(\sigma - \sigma_0(1 + v/c))^2/w^2\right)$$
$$V_A = B_0\sqrt{\pi w^2/4ln2}\exp\left(-\pi^2\Delta_A^2 w^2/4ln2\right) \tag{7}$$

$$I_A = I_0(1+U_A V_A cos\left(2\pi\sigma_0\left(\Delta_A(\sigma_0) + \left(\Delta_A(\sigma_0) + \sigma_0\frac{d\Delta_A}{d\sigma}\right)\frac{v}{c}\right)\right)$$
$$I_B = I_0(1+U_B V_B cos\left(2\pi\sigma_0\left(\Delta_B(\sigma_0) + \left(\Delta_B(\sigma_0) + \sigma_0\frac{d\Delta_B}{d\sigma}\right)\frac{v}{c}\right)\right)$$
$$I_C = I_0(1+U_C V_C cos\left(2\pi\sigma_0\left(\Delta_C(\sigma_0) + \left(\Delta_C(\sigma_0) + \sigma_0\frac{d\Delta_C}{d\sigma}\right)\frac{v}{c}\right)\right)$$
$$I_D = I_0(1+U_D V_D cos\left(2\pi\sigma_0\left(\Delta_D(\sigma_0) + \left(\Delta_D(\sigma_0) + \sigma_0\frac{d\Delta_D}{d\sigma}\right)\frac{v}{c}\right)\right) \tag{8}$$

$$v = \frac{(I_A - I_C)U_B cos\varphi_B + (I_B - I_A)U_C cos\varphi_C + (I_C - I_B)U_A cos\varphi_A}{(I_A - I_C)U_B\theta_B sin\varphi_B + (I_B - I_A)U_C\theta_C sin\varphi_C + (I_C - I_B)U_A\theta_A sin\varphi_A}C$$
$$where\ \varphi_k = 2\pi\sigma_0\Delta_k(\sigma_0),\ \ \theta_k = 2\pi\sigma_0\left(\Delta_k(\sigma_0) + \sigma_0\frac{d\Delta_k}{d\sigma}\right)\frac{v}{c},$$
$$k = (A, B, C, D) \tag{9}$$

The wind speed uncertainty is affected by the instrumental and emission line visibilities, the optical path difference, and the signal to noise ratio (SNR). SNR depends on the geometry of observation and the behaviour of the detector. Geometry of observation is schematically shown in Fig. 6. The instrument will fly in an orbit at about 325 km and take images of the limb of Mars (marked as gray area in Fig. 6). Light within an 8° × 8 field of view (FOV) will be collected by a 256 × 256 CCD. Each pixel of the CCD subtends a solid angle of 9.33 × 10^{-7} steradians, corresponding to a vertical resolution of 1.38 km at the tangent point of 40 km and 0.95 km at the tangent point of 190 km. 160 pixels will be binned together to improve the signal, at the cost of vertical and transverse resolution of the image and wind speed profiles. Thus, the image field will be a 150 km × 150 km square made up of 60 × 6 pixels each 2.5 km high.

Suppose the instrument has an aperture area A and locates at distance r from the emission volume, the total photon flux (P) received at a CCD pixel is the integration of selected Line VER (LVER) along the line of sight in the solid angle (Ω) the instrument extends ($\Omega = A/4\pi r^2$), shown in Eq. (10), where S_t and S_v denote the transverse and vertical resolution, respectively, τ is transmittance of the optical system, η is the quantum efficiency of the detector, and t is the integration time in second.

Table 4
A full set of glasses selected for MIMI.

Prism pairs	Arms	L (cm)	d_1 (cm)	d_2 (cm)	d_5 (cm)	$\partial\Delta/\partial T$ (cm K^{-1})	OPD (wavelength*)
K-LaSFn9/K-LaSFn10	K-PSK100	2.1407	12.658	12.723	1.5414	1.06e-5	0.795 + 1.03e5
K-LaSKn1/K-VC82							0.891 + 1.03e5
K-LaFn2/K-LaFK55	K-BOC20						0.087 + 1.03e5
K-GIR79/K-VC99							0.998 + 1.03e5

*The wavelength used for calculation here is 1.27 μm.

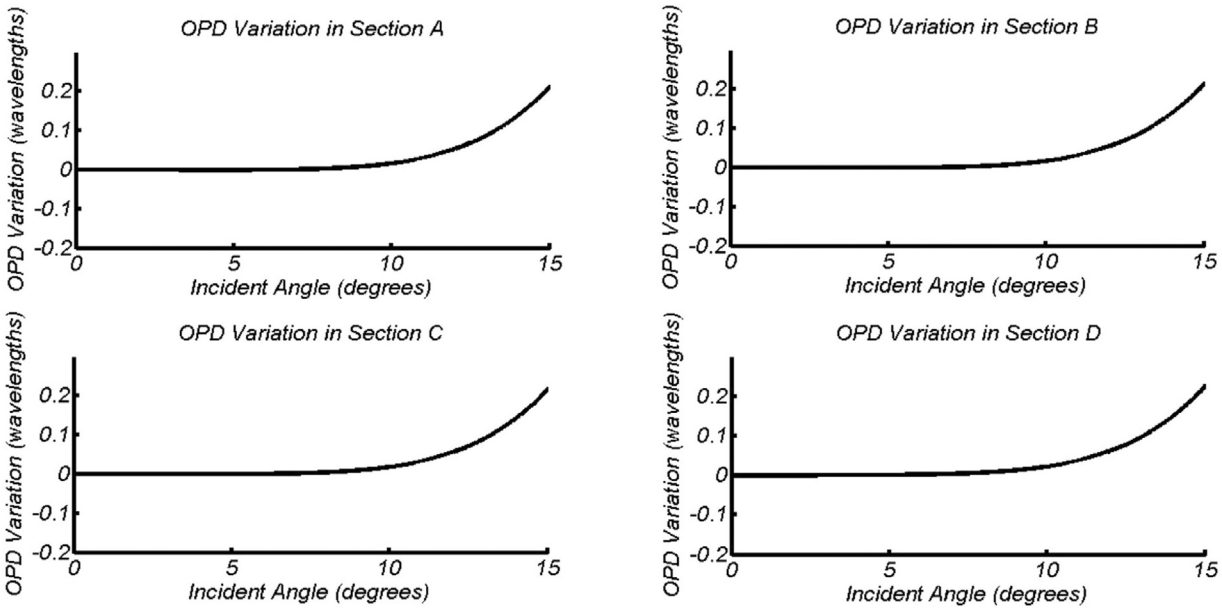

Fig. 5. OPD variations (in wavelength) with respect to incident angles (in degree) in four sections of MIMI.

visibility, V is the emission line visibility, and n is the number of

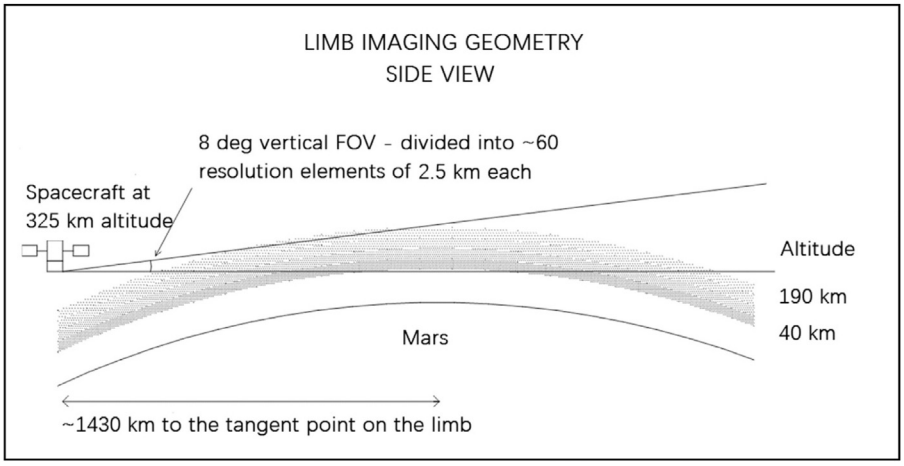

Fig. 6. Side view of limb imaging geometry (scale distorted).

$$P = \int (LVER)\Omega s_t s_v \tau \eta t dr \tag{10}$$

Omitting the dark current of the CCD for now to make the signal to noise ratio (SNR) simply the square root of the emission signal, the wind speed uncertainty is then derived using the standard deviation of measured phase shift of field-widened Michelson Interferometer (Eq. (11)), where c is the speed of light, λ is the wavelength of the target emission, Δ is the OPD, U is the instrumental pixels in a bin.

$$\delta v = c\lambda / 4\pi \Delta U \sqrt{P} \tag{11}$$

The instrument parameters for wind uncertainty estimation are summarized in Table 5.

The line of 1264.277 nm wavelength is used in the calculation because it is the weakest of the three selected lines and represents the worst case and maximum wind error. Substituting all these parameters into Eqs. (10) and (11), the estimated wind velocity

Table 5
Instrument parameters for wind uncertainty estimation.

Instrument parameters	Value
Aperture area (A)	18.49 cm^2
Instrumental visibility (U)	0.8
Emission line visibility (V)	0.8
Optical system transmittance (τ)	0.1
Integration time (t)	1 s
CCD quantum efficiency (η)	0.6
Line wavelength (λ)	1264.277 nm
OPD (Δ)	13 cm
Vertical resolution (s_v)	2.5 km
Transverse resolution (s_t)	25 km

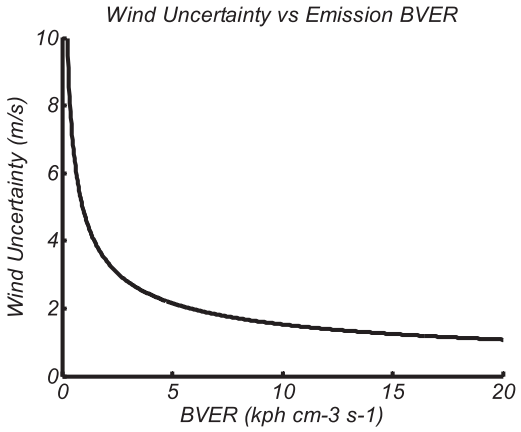

Fig. 7. Wind speed uncertainty (in m/s) variation with the BVER of O_2 nightglow on Mars (in kph cm^{-3} s^{-1}).

measurement uncertainty of MIMI as a function of target emission BVER is achieved. Fig. 7 shows that under our design the estimated wind speed uncertainty is smaller than 2 m/s when the emission BVER ranging from 5 to 20 kph cm^{-3} s^{-1}.

An accuracy of better than 10 m/s in wind measurement is the nominal value currently being considered acceptable for useful science [20]. Fig. 7 shows that MIMI can measure the wind with an accuracy better than 10 m/s when the BVER of O_2 nightglow is greater than 0.2 kph cm^{-3} s^{-1} and better than 2 m/s if it is greater than 5 kph cm^{-3} s^{-1}, which means the wind field in the whole interested region (40–80 km) (see Fig. 1) will be measured with a reasonable accuracy. Thus, we can safely conclude that the current design of MIMI is capable of accurate wind measurement.

6. Conclusion

MIMI–the Mars Imaging Michelson Interferometer is designed, as the first demonstration implementing the divided-mirror technique using refringent materials in a field-widened Michelson Interferometer, to observe the atmospheric dynamics at low latitudes of Mars by measuring $O_2(a^1\Delta_g)$ nightglow. Its optical layout and glass selection process are described, emphasising the features of monolithic construction, compactness, field widening, and thermal compensation. Its behaviour in measuring the target emission is analysed, using the wind velocity uncertainty as the primary criterion. MIMI can measure the wind with an accuracy better than 10 m/s if the BVER of O_2 nightglow is greater than 0.2 kph cm^{-3} s^{-1} and better than 2 m/s if it is greater than 5 kph cm^{-3} s^{-1}. Further research concerns the imaging capacity of MIMI when the incoming rays are out of the perpendicular plane of the prism sides and how that will affect the OPD of this instrument.

Acknowledgements

This work was supported by the National High Technology Research and Development Program of China (Grant no. 2012AA121101), the Major Program of the National Natural Science Foundation of China (Grant no. 41530422), the National Science and Technology Major Project of the Ministry of Science and Technology of the People's Republic of China (Grant no. 32-Y30B08-9001-13/15), and the National Natural Science Foundation of China (Grant no. 61275184, 61540018, 61405153). Support for W. Ward was provided through his NSERC Discovery Grant.

References

[1] Shepherd G. WINDII - the wind imaging interferometer on the upper atmosphere research satellite. J Geophys Res 1993;98(10):10725–50.
[2] Shepherd G. Application of Doppler Michelson imaging to upper atmospheric wind measurement: WINDII and beyond. Appl Opt 1996;35(16):2764–73.
[3] Shepherd G, Desaulniers M, Gault W, Hersom C, Smith K, Scott A, et al. Wind imaging interferometer on NASA's upper atmosphere research satellite. optical payloads for space missions. In: Shen-En Qian, editor. John Wiley and Sons; 2015.
[4] Gault W, Brown S, Moise A, Liang D, Sellar G, Shepherd G, et al. ERWIN: an E-region wind interferometer. Appl Opt 1996;35(16):2913–22.
[5] Kristoffersen S, Ward W, Brown S, Drummond J. Calibration and validation of the advanced E-region wind interferometer. Atmos Meas Tech 2013;6:1–16.
[6] Shepherd G, McDade I, Gault W, Rochon Y, Scott A, Rowlands N, et al. The stratospheric wind interferometer for transport studies (SWIFT). Adv Space Res 2001;27(6–7):1071–9.
[7] Langille J, Ward W, Scott A, Arsenault D. Measurement of two-dimensional Doppler wind fields using a field widened Michelson interferometer. Appl Opt 2013;52(8):1617–28.
[8] Gault W, Sargoytchev S, Shepherd GG. Divided-mirror scanning technique for a small Michelson mterferometer. Proc SPIE Int Soc Opt Eng 2001;4306:266–72.
[9] McCall S, Dobrowolski J, Shepherd G. Phase shifting thin film multilayers for Michelson interferometers. Appl Opt 1989;28(14):2854–9.
[10] Ward W, Gault W, Shepherd G, Rowlands N. Waves Michelson interferometer: a visible/near-IR interferometer for observing middle atmosphere dynamics and constituents. Proc SPIE Int Symposium Remote Sens 2001;4540:100–11.
[11] Babcock D. Mesospheric imaging michelson interferometer instrument development and observations Ph.D. Thesis. Toronto: York University; 2006.
[12] Krasnopolsky VA. Night and day airglow of oxygen at 1.27 μm on Mars. Planetary Space Sci 2013;85:243–9.
[13] Noxon JF. Auroral emission from $O_2(^1\Delta_g)$. J Geophys Res 1970;75(10):1879–91.
[14] Krasnopolsky VA. Mapping of Mars O_2 1.27 μm dayglow at four seasonal points. Icarus 2003;165:315–25.
[15] Guslyakova S, Fedorova A, Lefèvre F, Korablev O, Montmessin F, Trokhimovskiy A, et al. Long-term nadir observations of the O_2 dayglow by SPICAM IR. Planetary Space Sci 2016;122:1–12.
[16] Bertaux J-L, Gondet B, Bibring J-P, Montmessin F, Lefevre F. First detection of O_2 recombination nightglow emission at 1.27 μm in the atmosphere of mars With OMEGA / MEX and comparison with model. In: Fourth international workshop on the mars atmosphere: modelling and observations; 2011. p. 3 ⟨hal-00566300⟩.
[17] Fedorova A, Lefèvre F, Guslyakova S, Korablev O, Bertaux J-L, Montmessin F, et al. The O_2 nightglow in the martian atmosphere by SPICAM onboard of Mars-Express. Icarus 2012;219(2):596–608.
[18] Muñoz A, McConnell J, McDade I, Melo S. Airglow on Mars: some model expectations for the OH Meinel bands and the O_2, IR atmospheric band. Icarus 2005;176(1):75–95.
[19] Ward W, Gault W, Rowlands N, Wang S, Shepherd G, McDade I, et al. An imaging interferometer for satellite observations of wind and temperature on Mars, the dynamics atmosphere Mars observer (DYNAMO). In: Proceedings of SPIE - The International Society for Optical Engineering, vol. 4833; 2002. p. 226–36.
[20] Shepherd G G. Spectral imaging of the atmosphere.San Diego, Calif: Academic Press; 2002.
[21] Gault W, Sargoytchev S, Brown S. Divided mirror technique for measuring doppler shifts with a Michelson interferometer. Sensors Camera Syst Sci, Ind, Digital Photograp Appl II 2001;4306:266–72.
[22] Thuillier G, Shepherd G. Fully compensated Michelson interferometer of fixed path difference. Appl Opt 1985;24:1599–603.
[23] Gault W, Johnston S, Kendall D. Optimization of a field-widened Michelson interferometer. Appl opt 1985;24(11):1604–8.
[24] Rochon YJ. The retrieval of winds, doppler temperatures, and emission rates for the WINDII experiment. York University, Toronto; 2000 Ph.D. Thesis.
[25] Sumita Optical Glass. Inc.. Optical glass data book, version 9.01. 2015.
[26] Rahnama P, Rochon Y, McDade I, Shepherd G, Gault W, Scott A. Satellite measurement of stratospheric winds and ozone using doppler michelson interferometry. Part I instrument model and measurement simulation. J Atmosph Ocean Technol 2006;23:753–70.